SCIENCE CHINA
Physics, Mechanics & Astronomy

• Article •

July 2014 Vol. 57 No. 7: 1363–1375
doi: 10.1007/s11433-014-5479-0

Aerodynamic design optimization by using a continuous adjoint method

LUO JiaQi[1], XIONG JunTao[2] & LIU Feng[1,2*]

[1]*College of Engineering, Peking University, Beijing 100871, China;*
[2]*Department of Mechanical and Aerospace Engineering, University of California, Irvine, CA 92697-3975, United States*

Received April 16, 2013; accepted October 12, 2013; published online May 15, 2014

This paper presents the fundamentals of a continuous adjoint method and the applications of this method to the aerodynamic design optimization of both external and internal flows. General formulation of the continuous adjoint equations and the corresponding boundary conditions are derived. With the adjoint method, the complete gradient information needed in the design optimization can be obtained by solving the governing flow equations and the corresponding adjoint equations only once for each cost function, regardless of the number of design parameters. An inverse design of airfoil is firstly performed to study the accuracy of the adjoint gradient and the effectiveness of the adjoint method as an inverse design method. Then the method is used to perform a series of single and multiple point design optimization problems involving the drag reduction of airfoil, wing, and wing-body configuration, and the aerodynamic performance improvement of turbine and compressor blade rows. The results demonstrate that the continuous adjoint method can efficiently and significantly improve the aerodynamic performance of the design in a shape optimization problem.

continuous adjoint method, aerodynamic design optimization, transonic flow, computational fluid dynamics, aerospace engineering

PACS number(s): 02.60.Pn, 47.85.Gj, 47.85.lb

Citation: Luo J Q, Xiong J T, Liu F. Aerodynamic design optimization by using a continuous adjoint method. Sci China-Phys Mech Astron, 2014, 57: 1363–1375, doi: 10.1007/s11433-014-5479-0

1 Introduction

With the advances in computational power and numerical methods, research and application of aerodynamic design optimization (ADO) technologies based on computational fluid dynamics (CFD) have become very active and been widely used in aerospace engineering. At the beginning of this century, Jameson and Vassberg [1] forecasted that the advanced aerodynamic design methods would play the most important role in the design process of aerodynamic vehicles. In recent years, Airbus 380, Boeing 787, C919, M88 and PW4000 were designed by using the CFD-based design optimization and the aerodynamic performance was significantly improved with shortened design cycle and saved design cost.

In the CFD-based aerodynamic design optimization, the cost function defined to measure the performance of the aerodynamic shape is firstly determined through solving the governing flow equations in each design cycle. The aerodynamic shape is then redesigned by using the optimization method attempting to finally obtain the optimal shape with maximum aerodynamic performance and under required constraints. At present, the optimization methods can be categorized by non-gradient-based methods and gradient-based methods. Response surface method (RSM) [2–4] and genetic algorithm (GA) [5–8] are two of the non-gradient-based methods having been widely used in the aerodynamic design optimization. Recently Zhang et al. [9,10] successfully performed

*Corresponding author (email: fliu@uci.edu)

© Science China Press and Springer-Verlag Berlin Heidelberg 2014

design and optimization of the commercial airplane C919 of China by using GA. An acceptable optimization method should have excellent performance on obtaining the global optimal and increasing the optimization efficiency. The design optimization by using RSM and GA can efficiently support the global optimal. However, the number of the needed flow calculations depends strongly on the number of design parameters. For the design of complex configuration with a large number of design parameters by using either RSM or GA, the optimization efficiency is low and consequently it may usually be achieved only on a supercomputer. The finite-difference method (FDM) is one of the gradient-based methods and the implementation in the design optimization is simple. However, the number of needed flow calculations depends linearly on the number of design parameters and thus the optimization efficiency is not acceptable; and furthermore, the accuracy of FDM gradient can be significantly influenced by the step size used in the finite difference. Hereby it is rarely applied to the aerodynamic design optimization. In the late 1980s, Jameson et al. [11–13] proposed another gradient-based method, the adjoint method via the control theory of partial differential equations.

In the design optimization by using the adjoint method, the complete gradient information can be obtained by solving the governing flow equations and the corresponding adjoint equations only once for each cost function, regardless of the number of design parameters. Due to its high accuracy and high efficiency for gradient calculation, the adjoint method has been successfully used in the design optimization of external flows. Reuther et al. [14,15] performed a series of optimization designs of airfoil, wing, wing-body configuration by using the continuous adjoint method and successfully improved the aerodynamic performance of the aircraft of McDonnell Douglas. In recent years, the continuous adjoint formulation for unstructured grids [16] and the flutter control based on the adjoint method [17] were achieved. Xiong et al. [18–20] successfully performed inverse design and optimization designs of aero-elastic wings. Kim et al. [21] tuned an existing adjoint-based design method by adjusting the control parameters of CFD analysis and design process.

In the first few years of this century, Dreyer et al. [22], Liu et al. [23], and Wu et al. [24] introduced the adjoint method to the design optimization of internal flows. Because of the complexity of both flow conditions and geometries at the inlet and outlet boundaries of turbomachinery blade rows, work is required to determine the choice of cost functions and the appropriate boundary conditions for the adjoint equations. Luo et al. [25–27] studied the optimization through blade profile modification, spanwise restaggering and endwall contouring to effectively reduce the flow loss of turbine stators by using the continuous adjoint method. They also performed multipoint design optimization of a transonic compressor rotor to improve the overall performance in the whole operating range and the shock/tip-leakage interaction near stall [28]. Xiong et al. [29] successfully redesigned the fan-flow deflectors in the nozzle by using the adjoint method to effectively reduce jet noise. Wang et al. [30,31], Ji et al. [32] and Walther et al. [33] introduced a mixing-plane method to solve the adjoint equations in the design optimization of multi-stages. The adjoint method has also been applied to the aero-elastic design optimization of turbomachinery [34] and the design optimization based on an inverse method [35].

The continuous adjoint method has been used in the design optimization of both external and internal flows. More efforts are still required on the implementation and application of this optimization method in aerospace engineering. The present study will firstly introduce the fundamentals of the continuous adjoint method, and then present the general formulation of the adjoint equations and the corresponding boundary conditions. Secondly the crucial issues of design optimization, such as cost function and parameterization are briefly introduced. Finally a series of optimization design examples are presented, including an inverse design of airfoil and the aerodynamic design optimization of airfoil, wing, wing-body configuration, turbine stator and compressor rotor under single and multiple point design conditions.

2 The adjoint method

2.1 Fundamentals

Since the cost function I of aerodynamic design optimization is dependent on the flow field solution $\boldsymbol{w}$ and the geometry of aerodynamic shape $\mathcal{F}$, we write the cost function in the following general functional form

$$I = I(\boldsymbol{w}, \mathcal{F}). \tag{1}$$

Following the variation principle, eq. (1) can be written as:

$$\delta I = \frac{\partial I}{\partial \boldsymbol{w}}\delta \boldsymbol{w} + \frac{\partial I}{\partial \mathcal{F}}\delta \mathcal{F}. \tag{2}$$

The first and the second terms on the right-hand-side of the above equation represent the changes of cost function due to the variation of flow field solution and the modification of aerodynamic shape, respectively. The variation of flow field solution implicitly depends on the variation of aerodynamic shape through the governing flow equations, which may be generally represented by the following functional form

$$\boldsymbol{R}(\boldsymbol{w}, \mathcal{F}) = 0. \tag{3}$$

The gradient $\boldsymbol{G}$ can be defined as the variation of cost function δI per unit variation of aerodynamic shape $\delta \mathcal{F}$. From eq. (2) we have

$$\delta I = \boldsymbol{G}\delta \mathcal{F} = \left(\frac{\partial I}{\partial \mathcal{F}} + \frac{\partial I}{\partial \boldsymbol{w}}\frac{\partial \boldsymbol{w}}{\partial \mathcal{F}}\right)\delta \mathcal{F}. \tag{4}$$

From eq. (4) it is known that in order to obtain each of the gradient components, the variation of flow field solution responding to the variation of aerodynamic shape should be calculated. Hence at least $N + 1$ flow calculations are required to determine the complete gradient if the finite-difference

method is used, where N is the number of design parameters. By using this method, the computational effort is very costly when the number of design parameters is large.

The key of the adjoint method is to eliminate the influence of the variation of flow field solution $\delta \boldsymbol{w}$ on the gradient by introducing an adjoint operator and regarding the governing flow equation $\boldsymbol{R}$ as a constraint. Taking the variation of eq. (3), we obtain

$$\delta \boldsymbol{R} = \frac{\partial \boldsymbol{R}}{\partial \boldsymbol{w}} \delta \boldsymbol{w} + \frac{\partial \boldsymbol{R}}{\partial \mathcal{F}} \delta \mathcal{F} = 0. \tag{5}$$

Multiplying eq. (5) by a Lagrange operator Ψ and then subtracting it from eq. (2), we obtain

$$\delta I = \left\{ \frac{\partial I}{\partial \boldsymbol{w}} - \Psi^{\mathrm{T}} \frac{\partial \boldsymbol{R}}{\partial \boldsymbol{w}} \right\} \delta \boldsymbol{w} + \left\{ \frac{\partial I}{\partial \mathcal{F}} - \Psi^{\mathrm{T}} \frac{\partial \boldsymbol{R}}{\partial \mathcal{F}} \right\} \delta \mathcal{F}. \tag{6}$$

The explicit dependence of δI on $\delta \boldsymbol{w}$ can be eliminated by setting

$$\frac{\partial I}{\partial \boldsymbol{w}} - \Psi^{\mathrm{T}} \frac{\partial \boldsymbol{R}}{\partial \boldsymbol{w}} = 0. \tag{7}$$

Then the variation of the cost function with respect to the variation of aerodynamic shape can be determined by

$$\delta I = \boldsymbol{G} \delta \mathcal{F}, \tag{8}$$

where

$$\boldsymbol{G} = \frac{\partial I}{\partial \mathcal{F}} - \Psi^{\mathrm{T}} \frac{\partial \boldsymbol{R}}{\partial \mathcal{F}}. \tag{9}$$

Eq. (7) is called the adjoint equation to eq. (3). Eq. (9) gives the gradient of the cost function I to the aerodynamic shape $\mathcal{F}$.

In order to calculate the gradient as shown by eq. (9), the flow field $\boldsymbol{w}$ should be firstly obtained by solving eq. (3) and then obtain the adjoint flow field Ψ by solving eq. (7). In the CFD-based design optimization, the adjoint equation is similar to the governing flow equation in type and dimensions and thus requires the same level of computational effort for solution. Once the flow field $\boldsymbol{w}$ and the adjoint flow field Ψ are obtained, the gradient can then be calculated on obtaining additional derivatives of the cost function and computational grid metrics on the design parameters, which can be evaluated conveniently and with relatively small computational cost by a finite-difference scheme and by using the chain rule for derivatives. Hereby the adjoint method requires about twice the computation effort of flow calculation to obtain the complete gradient information for each cost function, regardless of the number of design parameters. Table 1 gives typical numbers of flow calculations needed in each design cycle for the optimization methods including second-order RSM, GA, FDM and adjoint method, where N is the number of design parameters. For GA, N is the number of populations and m is the number of individuals of each population. It is known from this table that the optimization efficiency by using the adjoint method is significantly higher than others.

Table 1 Number of flow calculations needed in each design cycle for different optimization methods

Method	RSM	GA	FDM	Adjoint
Number	N^2	$N \times m$	$N+1$	≈ 2

2.2 Continuous adjoint equations and boundary conditions

The derivations of the general formulation of the continuous adjoint equation and the boundary conditions corresponding to the three-dimensional Navier-Stokes equation are presented in this section. The Reynolds-Averaged Navier-Stokes (RANS) equation with a source term is usually given as:

$$\frac{\partial \boldsymbol{w}}{\partial t} + \frac{\partial (\boldsymbol{f}_j - \hat{u}_j \boldsymbol{w} - \boldsymbol{f}_{v,j})}{\partial x_j} - \boldsymbol{S} = 0, \quad j = 1, 2, 3, \tag{10}$$

where $\boldsymbol{f}_j$ and $\boldsymbol{f}_{v,j}$ are the inviscid and viscous fluxes, respectively; $\hat{u}_j$ and $\boldsymbol{S}$ denote the grid velocity and the source term, respectively. For three-dimensional flow with a grid attached to a rotor in the x-direction

$$\hat{u}_1 = 0, \quad \hat{u}_2 = -\Omega x_3, \quad \hat{u}_3 = \Omega x_2,$$
$$\boldsymbol{S} = \{0,\ 0,\ \rho u_3 \Omega,\ -\rho u_2 \Omega,\ 0\}^{\mathrm{T}},$$

where Ω is the rotation speed; u_j and x_j denote the absolute velocity and the cartesian coordinate in the physical domain, respectively. The addition of the above source term and grid velocity due to rotation is specific for turbomachinery applications.

Usually the cost function is defined on the boundary of the aerodynamic shape, the variation of which can be given as:

$$\delta I = \int_B \delta C \mathrm{d}B = \int_B \delta C_f \mathrm{d}B + \int_B \delta C_g \mathrm{d}B, \tag{11}$$

where C is a scalar function of both flow variables and geometric variables and depends on the definition of cost function; δC_f and δC_g denote the flow variation term and the geometric variation term, respectively, and $\delta C_f = \boldsymbol{c}^{\mathrm{T}} \delta \boldsymbol{w}$.

The governing flow equation is regarded as a constraint in the derivation of the adjoint equation. The variation of the steady-state RANS equations can be given as:

$$\frac{\partial (\delta \boldsymbol{F}_i - \delta \boldsymbol{F}_{v,i})}{\partial \xi_i} - \delta (J \boldsymbol{S}) = 0, \quad i = 1, 2, 3, \tag{12}$$

where $\boldsymbol{F}_i = S_{ij}(\boldsymbol{f}_j - \hat{u}_j \boldsymbol{w})$, $\boldsymbol{F}_{v,i} = S_{ij} \boldsymbol{f}_{v,j}$; ξ_i denotes the cartesian coordinate in the computational domain; $S_{ij} = J K_{ij}^{-1}$, K_{ij} is the transformation matrix defined by $K_{ij} = \partial x_i / \partial \xi_j$; J is the determinant of K_{ij}. Multiplying eq. (12) by the adjoint variable Ψ and then subtracting it from eq. (11), we have

$$\delta I = \int_B \boldsymbol{c}^{\mathrm{T}} \delta \boldsymbol{w} \mathrm{d}B + \int_B \delta C_g \mathrm{d}B - \int_D \Psi^{\mathrm{T}} \left[\frac{\partial (\delta \boldsymbol{F}_i - \delta \boldsymbol{F}_{v,i})}{\partial \xi_i} - \delta (J \boldsymbol{S}) \right] \mathrm{d}D. \tag{13}$$

According to Gauss theorem, eq. (13) can be written as:

$$\begin{aligned}\delta I = & \int_B \left[\boldsymbol{c}^{\mathrm{T}} - n_i \Psi^{\mathrm{T}}(\boldsymbol{A}_{s,j} - \boldsymbol{A}_{vs,j}) S_{ij}\right] \delta \boldsymbol{w} \mathrm{d}B \\ & + \int_D \left[\frac{\partial \Psi^{\mathrm{T}}}{\partial \xi_i} S_{ij} \delta(\boldsymbol{f}_j - \hat{u}_j \boldsymbol{w} - \boldsymbol{f}_{v,j}) + \Psi^{\mathrm{T}} J \delta \boldsymbol{S}\right] \mathrm{d}D \\ & + \delta I_g, \end{aligned} \tag{14}$$

where $\boldsymbol{A}_{s,j}$ and $\boldsymbol{A}_{vs,j}$ are the Jacobian matrices defined as:

$$\boldsymbol{A}_{s,j} = \frac{\partial \boldsymbol{f}_j}{\partial \boldsymbol{w}} - \hat{u}_j \boldsymbol{I}_e, \quad \boldsymbol{A}_{vs,j} = \frac{\partial \boldsymbol{f}_{v,j}}{\partial \boldsymbol{w}},$$

where $\boldsymbol{I}_e$ is the unit matrix; and

$$\begin{aligned}\delta I_g = & \int_B n_i \Psi^{\mathrm{T}}(\boldsymbol{f}_j - \hat{u}_j \boldsymbol{w} - \boldsymbol{f}_{v,j}) \delta(S_{ij}) \mathrm{d}B + \int_B \delta C_g \mathrm{d}B \\ & + \int_D \left[\frac{\partial \Psi^{\mathrm{T}}}{\partial \xi_i}(\boldsymbol{f}_j - \hat{u}_j \boldsymbol{w} - \boldsymbol{f}_{v,j}) \delta(S_{ij})\right] \mathrm{d}D \\ & + \int_D \Psi^{\mathrm{T}} \boldsymbol{S} \delta J \mathrm{d}D. \end{aligned} \tag{15}$$

Eq. (15) is the general formula for gradient calculation.

As mentioned before, the key of the adjoint method is to eliminate the contributions of $\delta \boldsymbol{w}$ to the adjoint gradient. By setting the second term on the right hand side of eq. (14) to zero we obtain the continuous adjoint equation to RANS equation

$$\boldsymbol{A}_{s,j}^{\mathrm{T}} \frac{\partial \Psi}{\partial x_j} + \boldsymbol{B}_s^{\mathrm{T}} \Psi + \frac{1}{J} [\boldsymbol{M}^{-1}]^{\mathrm{T}} \boldsymbol{Y} = 0, \quad j = 1, 2, 3, \tag{16}$$

where $\boldsymbol{B}_s^{\mathrm{T}} \Psi$ is the adjoint source term and $\boldsymbol{M}$ is the transformation matrix between the conservative flow variables $\boldsymbol{w}$ and the primary flow variables $\bar{\boldsymbol{w}} = \{\rho, u_1, u_2, u_3, p\}^{\mathrm{T}}$ with the definitions

$$\boldsymbol{B}_s = \frac{\partial \boldsymbol{S}}{\partial \boldsymbol{w}}, \quad \delta \bar{\boldsymbol{w}} = [\boldsymbol{M}^{-1}] \delta \boldsymbol{w}, \tag{17}$$

and $\boldsymbol{Y}$ is the primary adjoint operator. The detailed forms of $\boldsymbol{M}$ and $\boldsymbol{Y}$ are presented in ref. [25]. The continuous adjoint equation consists of a set of linear partial differential equations and can be numerically solved by using the same CFD method as that used for solving the governing flow equation.

The boundary conditions of the adjoint equation can be determined from the first term on the right hand side of eq. (14). The influence of flow variation on gradient can be eliminated by setting

$$\boldsymbol{c}^{\mathrm{T}} - n_i \Psi^{\mathrm{T}}(\boldsymbol{A}_{s,j} - \boldsymbol{A}_{vs,j}) S_{ij} = 0. \tag{18}$$

Although the adjoint equation as shown by eq. (16) keeps unchanged, the boundary conditions are different for different cost functions.

In the design optimization of external flows, the far field boundary is usually far enough away from the aerodynamic shape. It is acceptable to set $\Psi = 0$ on the far-field boundary. In the design optimization of internal flows, on the inlet and outlet boundaries the viscous effects can usually be neglected. For a particular case where the normal direction of the inlet and outlet boundary planes are parallel to the axial direction, i.e., $n_2 = 0$, $n_3 = 0$, the determination of the inlet and outlet boundary conditions depends on only the Jacobian matrix $\boldsymbol{A}_{s,1}$, and eq. (18) can thus be simplified to

$$\boldsymbol{c}^{\mathrm{T}} - n_1 \Psi^{\mathrm{T}} \boldsymbol{A}_{s,1} S_{11} = 0. \tag{19}$$

Eq. (19) presents a general formula of the inlet and outlet boundary conditions of the continuous adjoint equations suitable for the design optimization of both viscous and inviscid internal flows studied in the present paper. Refs. [26,28] present the boundary conditions of the adjoint equations with respect to several different cost functions.

3 The problem of aerodynamic design optimization

A complete CFD-based design optimization procedure consists of three main parts, parameterization of aerodynamic shape, flow calculation and optimization method. In the present study, the Euler equations or RANS equations with turbulence model are numerically solved to support the flow field solutions. At present the molecular viscosity, thermal conductivity including their turbulent contributions are frozen in performing the derivations of the adjoint equations in the present study.

In starting an aerodynamic design optimization, a proper cost function should be given to evaluate the aerodynamic performance. In the present study, the design optimization of external flows attempts to reduce the drag with constrained lift, while the design optimization of internal flows attempts to improve the adiabatic efficiency with aerodynamic constraints. The improvement of adiabatic efficiency can be measured by the reduction of entropy production in turbomachinery [36]. Several different cost functions are given in the following and will be used in the sample problems to be described later.

$$I = \frac{1}{2} \int_B (p - p_t)^2 \mathrm{d}B, \tag{20a}$$

$$I = C_D + \frac{1}{2} \Lambda_1 (A - A_0)^2 + \frac{1}{2} \Lambda_2 (C_L - C_{L,0})^2, \tag{20b}$$

$$I = C_D + \frac{1}{2} \Lambda (C_L - C_{L,0})^2, \tag{20c}$$

$$I = s_{\mathrm{gen}} + \Lambda |\bar{\beta} - \bar{\beta}_0|, \tag{20d}$$

$$I = s_{\mathrm{gen}} + \Lambda_1 |\sigma - 1| + \Lambda_2 |\hat{\pi} - 1|, \tag{20e}$$

where p and p_t are the calculated and target pressure distributions, respectively on the airfoil surface; C_L and C_D are the drag coefficient and lift coefficient, respectively; A denotes the airfoil area; $\bar{\beta}$ denotes the mass-averaged flow turning at the outlet of turbine stator blade row; σ and $\hat{\pi}$ are the ratios of mass flow rate and total pressure ratio, respectively at the

outlet of compressor rotor blade row; s_{gen} denotes the mass-averaged entropy production at the outlet. Their definitions are given as:

$$s_{\text{gen}} = \frac{\int_B n_i \rho u_j S_{ij} s \mathrm{d}B}{\int_B n_i \rho u_j S_{ij} \mathrm{d}B}, \quad s = c_v \ln \frac{p}{p_r} - c_p \ln \frac{\rho}{\rho_r}, \tag{21a}$$

$$\bar{\beta} = \frac{\int_B n_i \rho u_j S_{ij} \beta \mathrm{d}B}{\int_B n_i \rho u_j S_{ij} \mathrm{d}B}, \quad \tan\beta = \frac{u_t}{u_x}, \tag{21b}$$

$$\sigma = \frac{\dot{m}}{\dot{m}_0}, \quad \hat{\pi} = \frac{\pi}{\pi_0}, \quad \pi = \frac{p_{0,e}}{p_{0,i}}. \tag{21c}$$

p_r and ρ_r are the references of pressure and density, respectively; u_t and u_x are the velocity components in the circumferential and axial directions, respectively; $\dot{m}_0$ and π_0 denote the mass flow rate and total pressure ratio at the outlet of the reference rotor blade row; $p_{0,i}$ and $p_{0,e}$ denote the mass-averaged total pressure at the inlet and outlet, respectively.

In the constrained design optimization, each constraint can be regarded as one design objective. As shown by eqs. (20b)–(20e), constraints are enforced by incorporating penalty functions in the original cost functions. In this way the design optimization with constraints is converted into the design optimization without constraint.

In the design optimization involving profile modification of the aerodynamic shape, Hicks-Henne shape functions [37] are introduced. The coefficients of the shape functions are regarded as the design parameters.

$$\delta c(x) = \sum_{i=1}^{N} a_i b_i(x), \tag{22}$$

where a_i and $b_i(x)$ are the design parameters and shape functions, respectively; $\delta c(x)$ denotes the circumferential perturbation added to a reference aerodynamic shape; N is the number of design parameters. Figure 1 presents five different airfoils and 16 shape functions uniformly distributed along the unit chord. 4th, 8th, 12th and All denote the airfoils by imposing the perturbation from the fourth, eighth, twelfth shape function and all three of them, respectively on the upper surface of NACA0012 airfoil.

It is seen from Figure 1 that (1) the maximum perturbation appears at the corresponding control point for each shape function; (2) the shape function can influence the airfoil shape from the leading edge to the trailing edge; and (3) the perturbed aerodynamic shape is still smooth enough. Imposing the perturbation corresponding to each of the design parameters on the aerodynamic shape, the grid deformation can be achieved by using the perturbation technology [38], finally the corresponding gradient component can be calculated from eq. (15). Once the complete gradient is obtained, the design parameters can then be determined by using the steepest descent method

$$a_i = -l g_i, \tag{23}$$

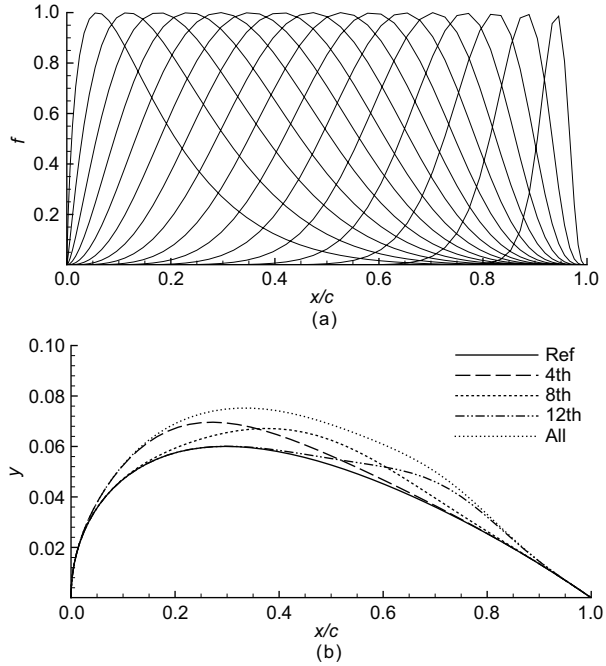


Figure 1 (a) Shape functions; and (b) perturbed airfoils.

where g_i denotes the i-th gradient component; l denotes the step length artificially given in the present study. On obtaining all the design parameters, the aerodynamic shape can then be updated by eq. (22).

In the design optimization of a turbine stator blade row, the blade cross-sectional profiles may be modified and the blade profile may be restaggered in the spanwise direction. Ref. [26] suggests a useful parameterization method for restaggering a three-dimensional blade in an annular blade row.

Figure 2 presents the process of the aerodynamic design optimization by using the continuous adjoint method. The design optimization stops when the cost function reaches an acceptable convergence. The steepest descent method is selected as the optimization method due to its simple and rapid implementation. Some other optimization methods may be used for obtaining the optimal with reduced total design cycles. However, more flow calculations and adjoint calculations are required in each design cycle.

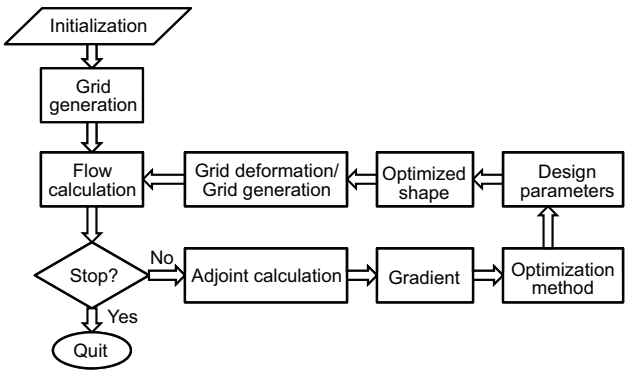


Figure 2 Process of the design optimization using the adjoint method.

4 Results and discussion

The following study presents a few important applications of the continuous adjoint method to the inverse design and the aerodynamic design optimization of both external and internal flows. The aerodynamic shapes including airfoil, wing, wing-body configuration, turbine stator and compressor rotor are optimized for proper cost functions.

4.1 Inverse design of airfoil

The inverse design attempts to determine the airfoil shape by specifying a pressure distribution, which is usually given based on the experience of the designers. Such an inverse problem may not always have a solution but may be converted to an optimization problem, in which the specified pressure distribution can be used as the target and an airfoil shape is sought to best approach the target pressure distribution. In the present test case, the target pressure distribution is predetermined from the airfoil RAE2822 and the inverse design starts from the reference airfoil NACA0012. The cost function is defined as eq. (20a). The flow conditions are given as $Ma = 0.734$, $Re = 6.5 \times 10^6$ and the attack angle $\alpha = 1.0°$. Since NACA0012 is a symmetric airfoil and RAE2822 is a supercritical airfoil, the starting and the target pressure distributions are quite different. This inverse design is performed to validate the effectiveness of the adjoint method in the aerodynamic design optimization. On each surface 16 shape functions are uniformly distributed.

In order to assess the accuracy of the gradients of the cost function with respect to the design parameters computed by the adjoint method, the same gradients are also calculated by the direct finite-difference method with different sizes of the perturbation dh normalized by the axial chord. The results are compared in Figure 3, where each of the gradients is normalized by the corresponding $L2$ norm. The FDM gradients with different perturbations converge and match well with the adjoint gradient except some minor differences around the shock on the upper airfoil surface.

On validating the accuracy of the adjoint method for computing the gradient, the optimization procedure of Figure 2 is then performed for this problem. After 50 design cycles, the normalized cost function decreases from unit to about 1.06×10^{-2}. The lift coefficient increases from 0.4437 to 0.7999, while the drag coefficient slightly increases from 0.0091 to 0.0104. Both the lift coefficient and the drag coefficient of the optimized airfoil approach close to those of the target airfoil, 0.8013 and 0.0112, respectively.

Figure 4 presents the pressure distributions and the shapes of the reference, the optimized and the target airfoils. The shape and the pressure distribution of the optimized airfoil are very close to the targets except minor differences around the shock.

Once the target pressure distribution is given, the optimized airfoil can be obtained fast and accurately through this optimization-based inverse design. An advantage of this optimization-based inverse design method is that the method will always yield a best solution whether the inverse problem has a solution or not.

4.2 Drag reduction of airfoil

In order to improve the commercial benefits of airplane, it is significant and necessary to reduce the drag of the airfoil with constrained lift. The shape and the attack angle of the NACA64A410 airfoil are optimized in the present design case. The cost function is defined as eq. (20b). The flow conditions are given as $Ma = 0.75$, $Re = 6.5 \times 10^6$ and the reference attack angle $\alpha = 1.0°$. On each surface 23 shape functions are uniformly distributed.

After 100 design cycles, the attack angle decreases to about 0.93°. Figure 5 presents the lift and drag coefficients versus design cycle. The drag coefficient of the optimized airfoil decreases from 0.02410 to 0.01155, a 52.1% reduction. The lift coefficient keeps almost unchanged.

Figure 6 presents the pressure distributions and the shapes of the reference and the optimized airfoils. Compared to the reference pressure distribution, the shock on the optimized airfoil almost disappears. Due to the geometric constraint,

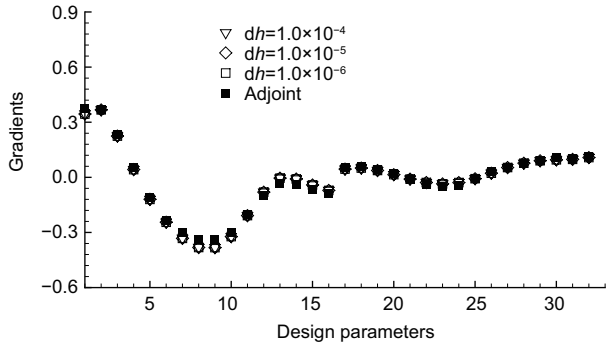


Figure 3 Comparisons of gradients.

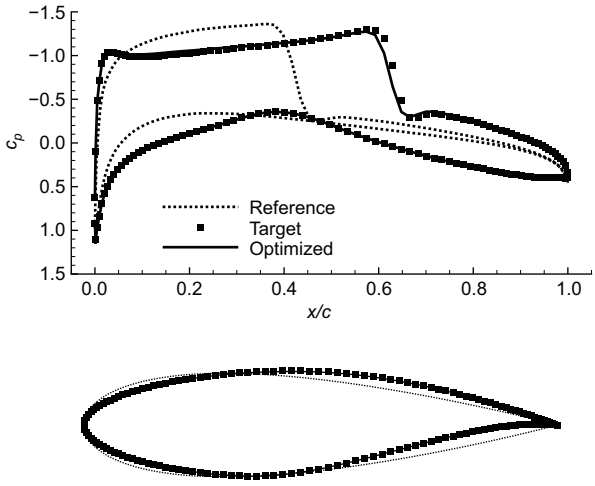


Figure 4 Comparisons of pressure distributions and airfoil shapes.

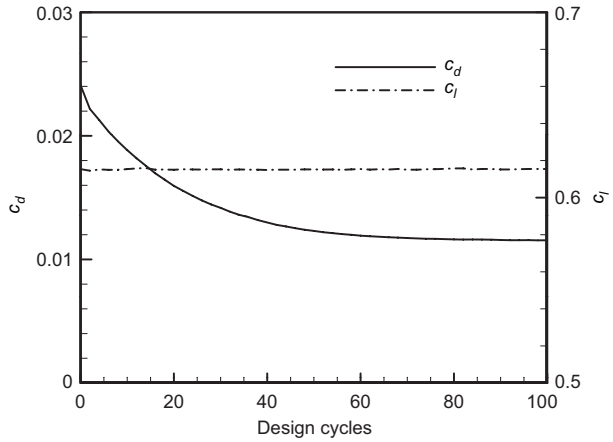


Figure 5 Coefficients of lift and drag versus design cycle.

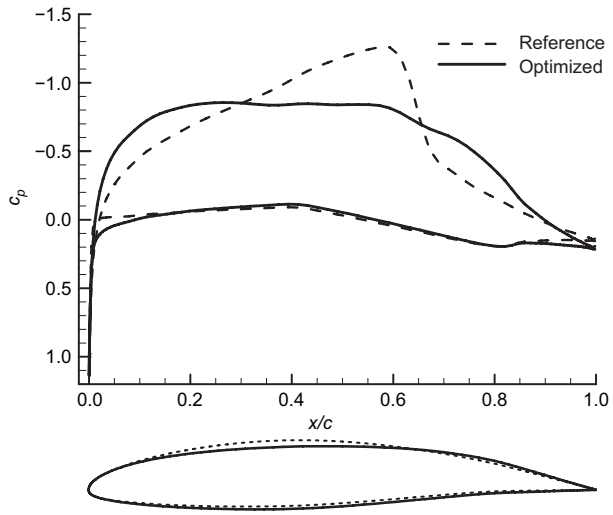


Figure 6 Comparisons of pressure distributions and airfoil shapes.

the thickness of the optimized airfoil decreases on the front portion and increases on the rear.

4.3 Drag reduction of wing

The shape and the attack angle of the supercritical Lann wing are optimized in the present design case to reduce the drag with constrained lift coefficient. The cost function is defined as eq. (20c). The aspect ratio of Lann wing is 7.92, the relative thickness is 12% and the semi-span length is 1.0 m. The flow conditions are given as $Ma = 0.82$ and the reference attack angle $\alpha = 0.56°$. Seven control sections along the span are selected to be optimized and 13 shape functions are uniformly distributed on each surface of the control sections and there are totally 182 design parameters.

After 45 design cycles, the optimized attack angle increases to about 0.565°. Figure 7 presents the lift and drag coefficients versus design cycle. The drag coefficient of the optimized airfoil decreases from 0.01134 to 0.00927. It decreases by 18.3%. The lift coefficient of the optimized airfoil remains almost the same as that of the reference airfoil.

Figure 8 presents the pressure distributions and the shapes of four different control sections for both the reference and the optimized wings, where b denotes the span. In this figure, the shock of the optimized wing is significantly weakened and hence the wave drag can be reduced. Figure 9 presents the pressure contours on the upper surface of the wings. The shock almost disappears on the whole upper surface of the optimized wing.

4.4 Drag reduction of wing-body configuration

In this subsection we demonstrate the application of the adjoint method to a wing-body configuration and also multi-

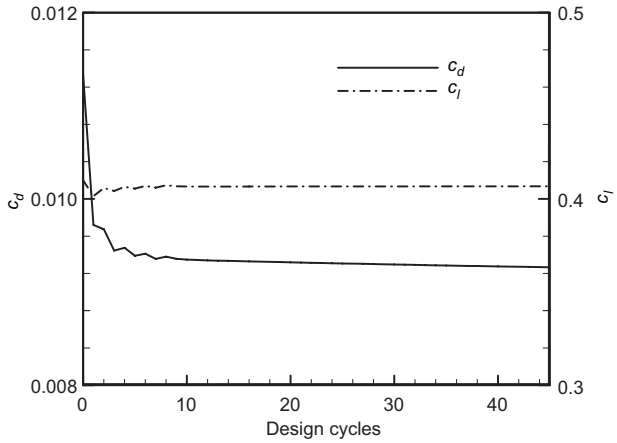


Figure 7 Coefficients of lift and drag versus design cycle.

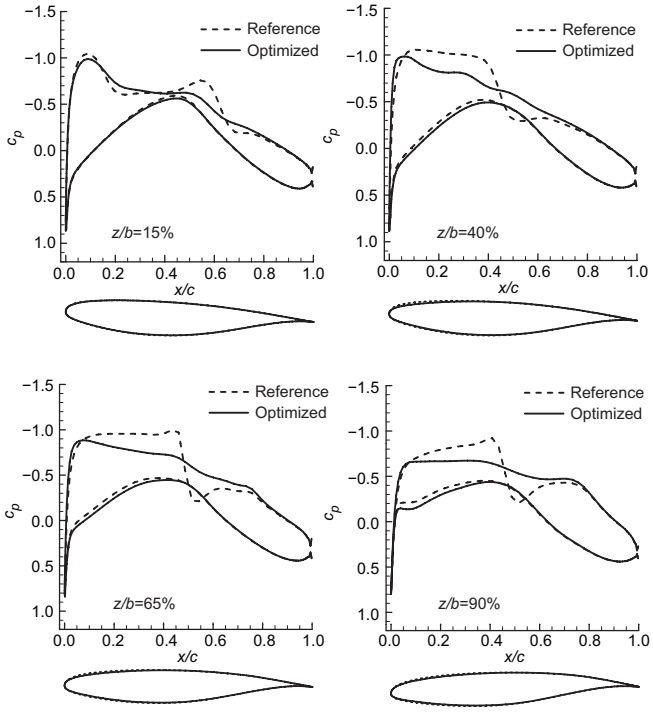


Figure 8 Shapes and pressure distributions at different span locations of the wings.

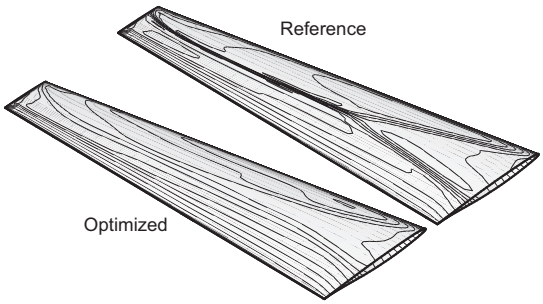


Figure 9 Pressure contours on the upper surface of the wings.

point design optimization. The cost function and the corresponding variation of the M design point optimization can be defined as:

$$I = \sum_{i=1}^{M} \lambda_i I_i, \quad \delta I = \sum_{i=1}^{M} \lambda_i \delta I_i, \tag{24}$$

where M is the number of design points, and λ_i is the weight for the i-th design point. In the present test case, the shape of the wing-body configuration DLR-F4 is optimized at three different design conditions with Mach number 0.72, 0.77 and 0.81 and the corresponding weights 0.3, 0.2 and 0.5, respectively. The given set of the weights constitutes only one test case. Designers can choose different sets of these parameters according to different requirements for industrial application. The Reynolds number is 3.0×10^6. The cost function at each design condition is defined as eq. (20c) with $C_{L,0} = 0.5$. Four control sections along the span are selected to be optimized and 13 shape functions are uniformly distributed on each surface of the control section.

Figure 10 presents the cost function versus design cycle. Figure 11 presents the pressure distributions and the shapes of two selected control sections for both the reference and the optimized configurations at three different design conditions. Figure 12 presents the drag coefficient at different Mach numbers for the reference and the optimized configurations. The drag coefficient can be significantly reduced at high Mach number, while it keeps almost unchanged at low Mach number. The results demonstrate that the multi-point design optimization of wing-body configuration by using the continuous adjoint method is effective.

4.5 Design optimization of a turbine stator

Compared to external flows, turbomachinery flow is much more complex because of the complex internal geometry, the relative motion of the blades, and the multi-stage configuration of the machine. As more and more high-level requirements need to be satisfied in aerospace engineering, the aerodynamic design optimization of turbomachinery becomes more and more significant and active nowadays. In the present design case, a turbine stator blade row is optimized to reduce the flow loss through blade profiling and restaggering along the span. The mass-averaged flow turning at the outlet is enforced to be equal to that of the reference blade. Hereby the adiabatic efficiency can be improved due to the reduction of flow loss without loss in working capability. The cost

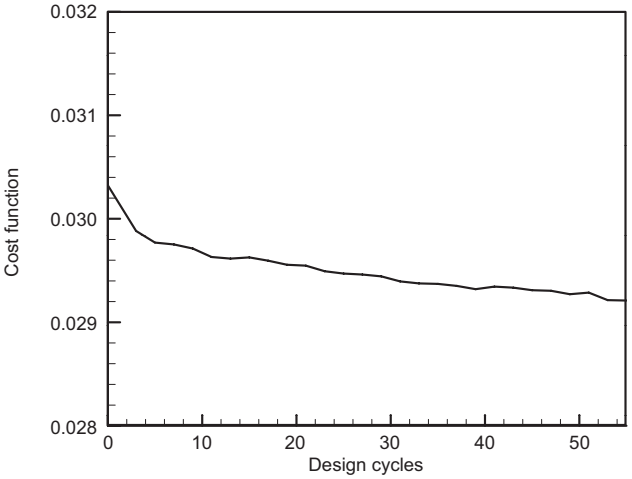


Figure 10 Cost function versus design cycle.

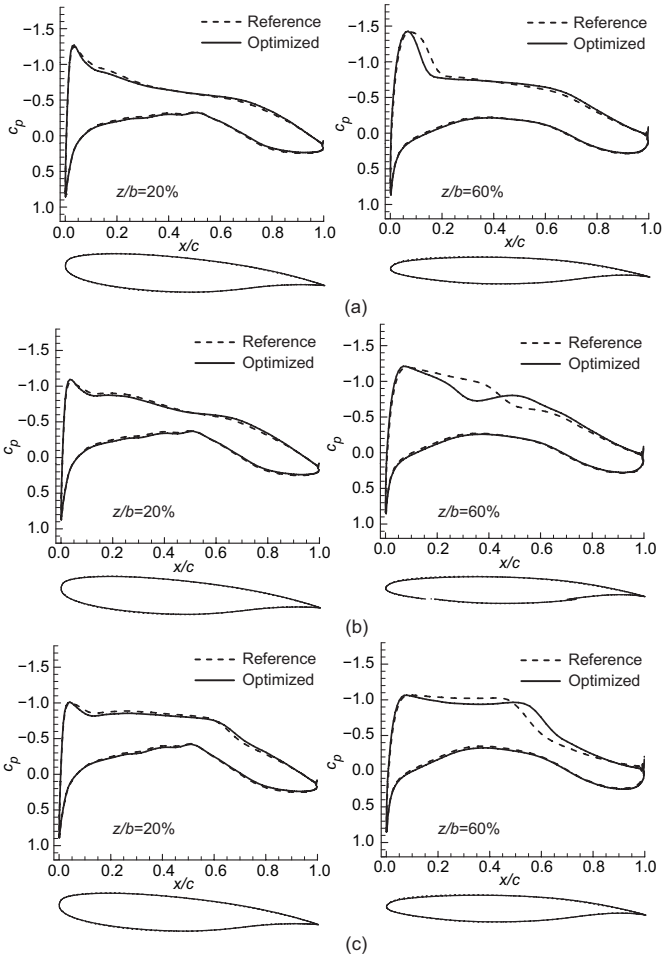


Figure 11 Shapes and pressure distributions of the wings at different design conditions: (a) $Ma = 0.72$; (b) $Ma = 0.77$; and (c) $Ma = 0.81$.

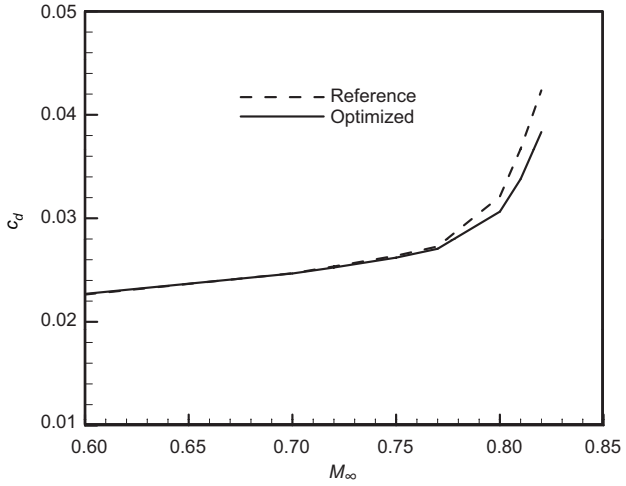


Figure 12 Drag coefficient at different Mach number with $C_L = 0.5$.

function is defined as eq. (20d) and $\Lambda = 20$. The three-dimensional Euler equations are selected as the governing flow equations. The stacking line of the stator blade is located at the trailing edge.

Table 2 gives the aerodynamic performance including normalized entropy production, normalized mass flow rate, flow turning, total pressure and adiabatic efficiency at the outlet of the reference and the optimized blades. For the optimized blade, the entropy production is decreased by 28.3%; the total pressure and adiabatic efficiency are increased by 0.52% and 0.70%, respectively; the mass flow rate is increased by 0.6%, while the flow turning remains almost unchanged due to the strictly enforced constraint.

Figure 13 presents the spanwise distributions of total pressure, adiabatic efficiency, flow turning, and stagger angle change represented by $\delta\alpha$. The total pressure, adiabatic efficiency and stagger angle of the optimized blade are increased over the whole blade span, while the flow turning decreases on the inner span and increases on the outer span.

Figure 14 presents the contours of isentropic Mach number on the suction surface and the contours of the circumferentially mass-averaged total pressure on the meridian plane. The shock on the optimized suction surface is significantly weakened and hence the total pressure increases on the whole blade span due to the performance improvement.

In order to study the effectiveness of the design optimization, Figure 15 presents both the inviscid and viscous performance of the reference and the optimized blades at off-design conditions. It is seen that (1) the operating range is wider for the optimized blade; (2) the performance of the optimized blade is improved at all of the off-design conditions; and (3) although the design optimization is performed without the influence of viscosity, the performance of the optimized blade keeps a similar relative improvement over the reference blade under viscous conditions.

Table 2 Performance of the reference and the optimized stator blades

	s_{gen}	$\dot{m}$	β (°)	$p_{0,e}/p_0$	η (%)
Reference	1.000	1.000	75.81	0.9821	97.61
Optimized	0.717	1.006	75.83	0.9872	98.29

4.6 Design optimization of a compressor rotor

The performance of the compressor rotor significantly influences the overall performance of an aircraft engine. With a given rotation speed and flow capacity, the compression ratio of the compressor rotor is usually fixed according to the overall performance. In this case the design optimization can be performed to increase the adiabatic efficiency and thus decrease the specific fuel consumption (SFC) of the engine. A

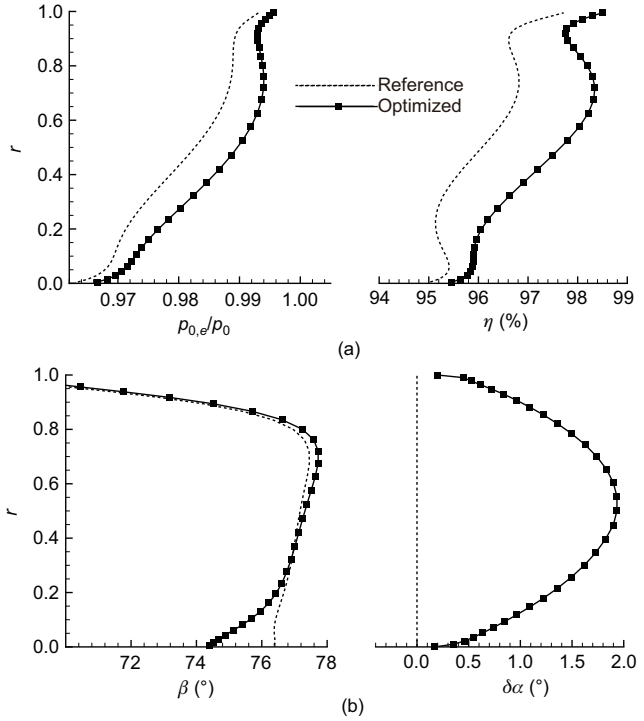


Figure 13 Spanwise distributions of: (a) total pressure and adiabatic efficiency; and (b) flow turning and stagger angle change.

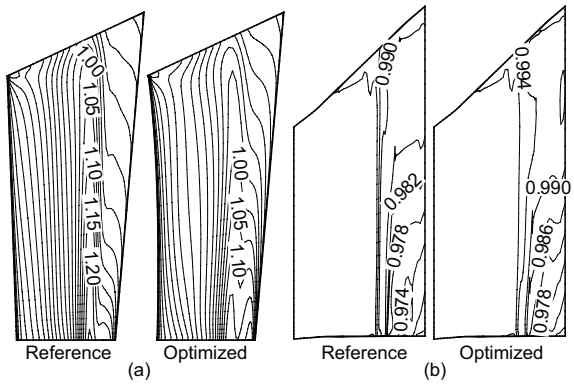


Figure 14 Contours of: (a) isentropic Mach number on the suction surface; and (b) total pressure on the meridian plane.

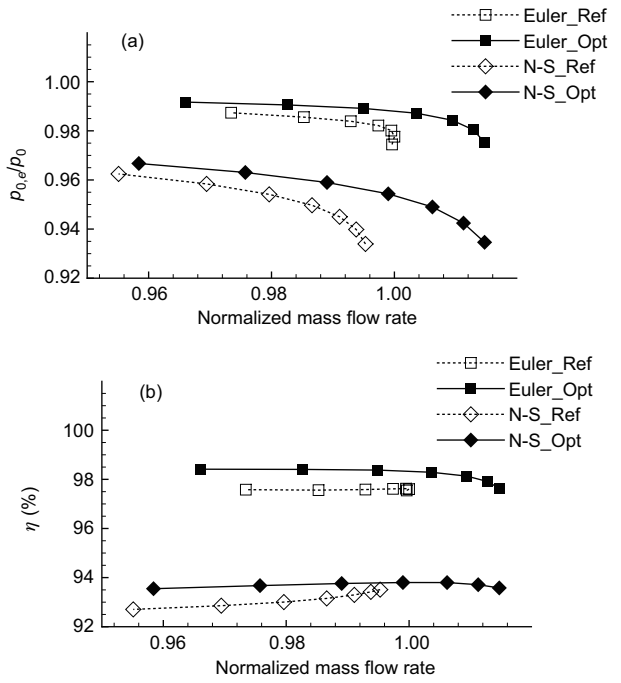


Figure 15 Performance at off-design conditions: (a) total pressure; and (b) adiabatic efficiency.

transonic compressor rotor blade row, the NASA Rotor 67, is optimized near peak efficiency (P.E.) in the present design case with constrained total pressure ratio and mass flow rate. The cost function is defined as eq. (20e) with $\Lambda_1 = 1.6$ and $\Lambda_2 = 0.15$. The profiles of nine different blade sections along the span are selected to be optimized and 16 shape functions are uniformly distributed on each blade surface. The three-dimensional RANS equations with one-equation turbulence model [39] is numerically solved to obtain the flow field [28].

Table 3 gives the performance including normalized entropy production, mass flow rate, total pressure ratio, adiabatic efficiency, and flow turning at the outlet of the reference and the optimized blades. Through optimizing the blade profiles, the entropy production is decreased by 13.4%, the adiabatic efficiency is increased by 1.10%, and the flow turning is slightly decreased. The total pressure ratio and the mass flow rate keep almost unchanged due to the strictly enforced constraints.

Figure 16 presents the contours of relative isentropic Mach number on the blade surface. The shock on the blade surface is significantly weakened for the optimized blade. The downstream pressure on the inner span of the optimized blade increases near the trailing edge.

Figure 17 presents the profiles and isentropic Mach number distributions at three different span locations of the reference and the optimized blades. Through blade profiling, the loading keeps almost unchanged on both 25% and 60% spans and decreases on 95% span, the shock at 60% and 95% span locations is significantly weakened. Especially at 95% span, the single shock of the reference blade is replaced by a double-shock system of the optimized blade. Denton and Xu [40], Biollo and Benini [41] pointed out that such a solution favors the reduction of aerodynamic loss associated with the shock, providing a more efficient local flow diffusion.

Figure 18 presents the spanwise distributions of total pressure ratio, adiabatic efficiency and flow turning. The total pressure ratio decreases on the outer span and increases on the inner span. The flow turning slightly decreases on the outer span and keeps unchanged on the inner span. The adiabatic efficiency increases on the whole span.

Table 3 Performance of the reference and the optimized rotor blades

	s_{gen}	$\dot{m}$ (kg/s)	π	η (%)	β (°)
Reference	1.000	34.59	1.627	92.09	−38.85
Optimized	0.866	34.59	1.626	93.10	−38.64

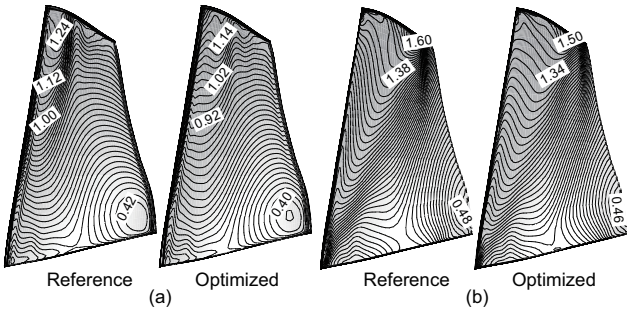


Figure 16 Contours of relative isentropic Mach number on the blade surface: (a) pressure side; and (b) suction side.

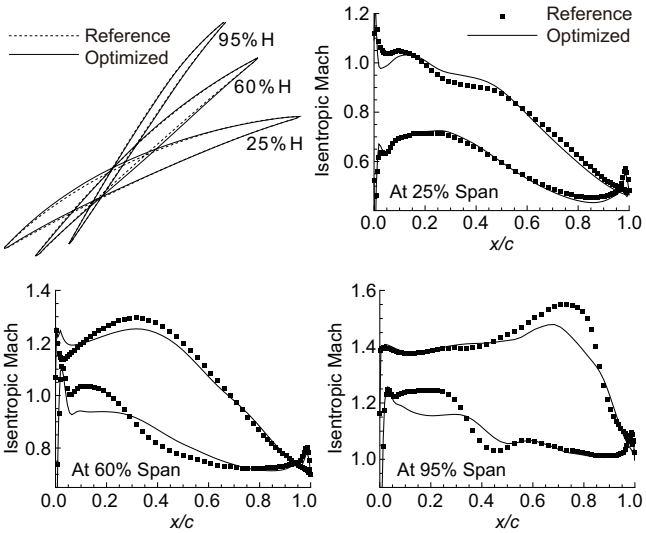


Figure 17 Blade profiles and distributions of relative isentropic Mach number on different spans.

4.7 Multi-point optimization of a compressor rotor

The aerodynamic performance at the operating condition near P.E. can be significantly improved through blade redesign. However, it is uncertain whether the performance at off-design conditions can be improved or not. In order to improve

the aerodynamic performance in a wider operating range, Rotor 67 is redesigned for three operating conditions, near choke, near P.E., and near stall in this design case.

Figure 19 gives the overall performance of the reference blade, the single and multi-point optimized blades. It is seen that (1) significant gains of adiabatic efficiency can be obtained from single-point optimization without any loss of total pressure ratio around the 98% normalized mass flow rate and beyond, however, for the mass flow rate below the 98% mark the total pressure ratio significantly decreases; and (2) the total pressure ratio of the multi-point optimized blade matches well that of the reference blade, while the adiabatic efficiency shows a significant increase in the whole operating range.

Shock/tip-leakage interaction is regarded as one of the main stall triggers in transonic compressor rotors. Suder et al. [42] and Chima [43] suggest that there exists a low dynamic head flow region along with severe flow blockage in the tip gap. In the present study relative Mach number is used to identify the flow blockage induced by shock/tip-leakage interaction. Figure 20 presents the contours of relative Mach number on the S1 streamsurface at the blade tip at the operating conditions near P.E. and near stall. Under the operating condition near P.E., the regions of low dynamic head are significantly reduced for the optimized blades due to the weakened shock on the outer span. Under the operating condition near stall, the single-point optimization makes little change to the shock/tip-leakage interaction. However, it is clear that the region of low dynamic head is reduced for the multi-point optimized blade. Although the true stall can not be captured in the present study, the shock/tip-leakage interaction near stall is indeed improved in the multi-point optimization, which helps increasing the stall margin.

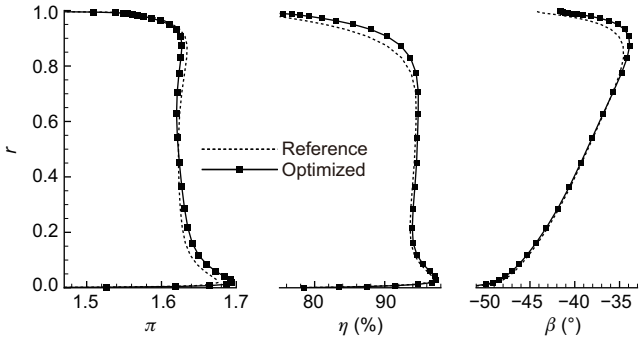


Figure 18 Spanwise distributions of total pressure ratio, adiabatic efficiency and flow turning.

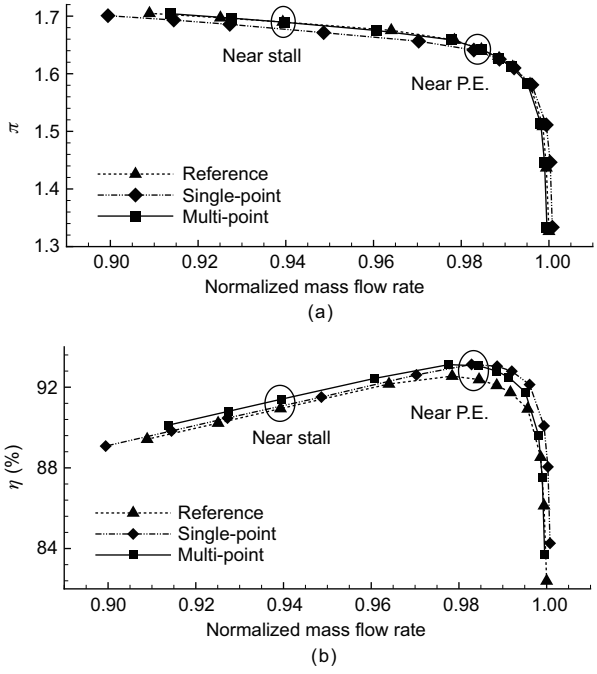


Figure 19 Performance at off-design conditions: (a) total pressure ratio; and (b) adiabatic efficiency.

5 Conclusion

This paper presents the general formulation of the continuous adjoint equations, in particular the derivation of the adjoint equations for the RANS equations, and the boundary conditions for the design optimization of both external and internal flows. The accuracy of the adjoint gradient and the effectiveness of the adjoint method are demonstrated for several different design cases including drag reduction of airfoil, wing and wing-body configuration and improvement of the adiabatic efficiency of turbine stator and compressor rotor blade rows. The results of the aerodynamic design optimization by using the continuous adjoint method in the present paper demonstrate

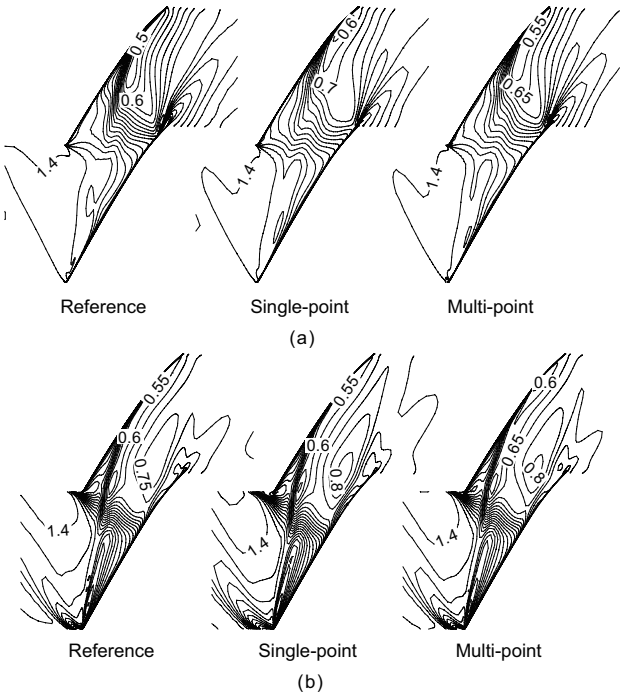


Figure 20 Leakage flow on the S1 streamsurface at the blade tip: (a) near P.E.; and (b) near stall.

(1) In each design cycle, the complete gradient information can be obtained by solving the governing flow equations and the corresponding adjoint equations only once for each cost function, regardless of the number of design parameters. This method with high-efficiency for gradient calculation is particularly useful for the design optimization of complex configuration with a large number of design parameters.

(2) In the multi-point design optimization, one cost function can be defined by the sum of all the weighted objectives to simplify the design optimization.

(3) The constraints can be imposed by adding the penalty functions in the original cost function and thus the design optimization with constraints can be converted into the design optimization without constraint.

By using the adjoint method, the computation effort for the aerodynamic design optimization can be significantly reduced. Due to its high accuracy and high efficiency for gradient calculation, this optimization method offers a powerful tool for wide application in aerodynamic design. However, it must be pointed out that the adjoint method is one of the gradient-based methods and only the local optimal can be obtained by using this method. Therefore, it is very suitable for application in the detailed design phase. In the preliminary design phase, the aerodynamic shape usually changes a lot, but a hybrid optimization method consisting of the adjoint method and other non-gradient-based methods, such as GA and RSM, may offer a better choice.

This work was supported by the National Natural Science Foundation of China (Grant Nos. 51206003 and 51376009) and the National Science Foundation for Post-doctoral Scientists of China (Grant Nos. 2012M510267 and 2013T60035).

1 Jameson A, Vassberg J C. Computational fluid dynamics for aerodynamic design: Its current and future impact. AIAA-2001-0538
2 Xiong J, Qiao Z, Han Z. Optimum aerodynamic design of transonic wing based on response surface methodology. Acta Aeronaut Et Astronaut Sin, 2006, 27: 399–402
3 Samad A, Kim K Y, Goel T, et al. Multiple surrogate modeling for axial compressor blade shape optimization. J Propul Power, 2008, 24: 301–310
4 Bonaiuti D, Zangeneh M. On the coupling of inverse design and optimization techniques for the multiobjective, multipoint design of turbomachinery blades. J Turbomach, 2009, 131: 021014
5 Larocca F. Multiple objective optimization and inverse design of axial turbomachienry blades. J Propul Power, 2008, 24: 1093–1099
6 Song L, Li J, Feng Z, et al. Multi-objective optimization design of the 3D transonic compressor cascade. J Eng Thermophys, 2007, 28: 223–225
7 Luo C, Song L, Li J, et al. Multi-objective and multidisciplinary optimization design method of turbomachinery blade. J Eng Thermophys, 2009, 30: 1651–1654
8 Öksüż Ö, Akmandor I S. Multi-objective aerodynamic optimization of axial turbine blades using a novel multilevel genetic algorithm. J Turbomach, 2010, 132: 041009
9 Zhang Y, Chen H, Zhang M, et al. Supercritical wing design and optimization for transonic civil airplane. AIAA 2011-27
10 Zhang Y, Chen H, Fu S, et al. A practical optimization methodology for transport aircraft wing/nacelle integration design. Acta Aeronaut Et Astronaut Sin, 2012, 33: 1993–2001
11 Jameson A. Aerodynamic design via control theory. J Sci Comput, 1988, 3: 233–260
12 Jameson A, Reuther J. Control theory based airfoil design using the Euler equations. AIAA 94-4272
13 Jameson A. Aerodynamic Shape Optimization Using the Adjoint Method. Technical Report, von Karmann Institute, 2003
14 Reuther J, Jameson A. Aerodynamic shape optimization of wing and wing-body configurations using control theory. AIAA 95-0123
15 Reuther J, Jameson A, Farmer J. Aerodynamic shape optimization of complex aircraft configurations via an adjoint formulation. AIAA 96-0094
16 Jameson A, Shankaran S, Martinelli L. Continuous adjoint method for unstructured grids. AIAA J, 2008, 46: 1226–1239
17 Palaniappan K, Sahu P, Jameson A, et al. Design of adjoint-based laws for wing flutter control. J Aircraft, 2011, 48: 331–335
18 Xiong J, Qiao Z, Yang X, et al. An efficient transonic inverse design method for aeroelastic wing. J Northwest Polytech Univ, 2007, 25: 12–16
19 Xiong J, Qiao Z, Yang X, et al. Optimum aerodynamic design of transonic wing based on viscous adjoint method. Acta Aeronaut Et Astronaut Sin, 2007, 28: 281–285
20 Xiong J, Qiao Z, Yang X, et al. An aerodynamic shape optimization of transonic wing design method for aeroelastic system. Acta Aerodyn Sin, 2009, 27: 154–159
21 Kim S, Hosseini K, Leoviriyakit K, et al. Enhancement of class of adjoint design methods via optimization of parameters. AIAA J, 2010, 48: 1072–1076
22 Dreyer J J, Martinelli L. Hydrodynamic shape optimization of propulsor configurations using a continuous adjoint approach. AIAA 2001-2580
23 Yang S, Wu H, Liu F, et al. Optimum aerodynamic design of cascades by using an adjoint equation method. AIAA 2003-1068
24 Wu H, Liu F, Tsai H M. Aerodynamic design of turbine blades using an adjoint equation method. AIAA 2005-1006
25 Luo J, Xiong J, Liu F, et al. Secondary flow reduction by blade redesign and endwall contouring using an adjoint optimization method. ASME GT2010-22061
26 Luo J, Xiong J, Liu F, et al. Three-dimensional aerodynamic design optimization of a turbine blade by using an adjoint method. J Turbomach, 2011, 133: 011026
27 Luo J, Liu F, McBean I. Optimization of endwall contours of a turbine blade row using an adjoint method. ASME GT2011-46163
28 Luo J, Zhou C, Liu F. Multi-point design optimization of a transonic compressor blade by using an adjoint method. ASME GT2013-95155
29 Xiong J, Liu F, Papamoschou D. Aerodynamic shape optimization of fan-flow deflectors for noise reduction using adjoint method. AIAA 2010-4675
30 Wang D, He L. Adjoint aerodynamic design optimization for blades in multi-stage turbomachines. Part I: methodology and verification. J Turbomach, 2010, 132: 021011
31 Wang D, He L, Li Y S, et al. Adjoint aerodynamic design optimization for blades in multi-stage turbomachines. Part II: validation and

application. J Turbomach, 2010, 132: 021012
32 Ji L, Yi W, Li W, et al. Multi-stage turbomachinery blades optimization design using adjoint method and thin shear-layer N-S equations. ASME GT2012-68537
33 Walther B, Nadarajah S. Constrained adjoint-based aerodynamic shape optimization of a single-stage transonic compressor. J Turbomach, 2013, 135: 021017
34 He L, Wang D. Concurrent blade aerodynamic aero-elastic design optimization using adjoint method. J Turbomach, 2011, 133: 011021
35 Yang J, Huang X, Wu H. Multi-row inverse method based on the adjoint optimization. ASME GT2011-46130
36 Denton J D. The 1993 IGTI scholar lecture: Loss mechanisms in turbomachines. J Turbomach, 1993, 115: 621–656
37 Hicks R M, Henne P A. Wing design by numerical optimization. J Aircraft, 1978, 15: 407–412
38 Liu F, Cai J, Zhu Y, et al. Calculation of wing flutter by a coupled fluid-structure method. J Aircraft, 2001, 38: 334–342
39 Spalart P R, Allmaras S R. A one-equation turbulence model for aerodynamic flows. AIAA 92-0439
40 Denton J D, Xu L. The effects of lean and sweep on transonic fan performance. ASME GT2002-30327
41 Biollo R, Benini E. Shock/boundary-layer/tip-clearance interaction in a transonic rotor blade. J Propul Power, 2009, 25: 668–677
42 Suder K L, Celestina M L. Experimental and computational investigation of the tip clearance flow in a transonic axial compressor rotor. J Turbomach, 1996, 118: 218–229
43 Chima R V. Calculation of tip clearance effects in a transonic compressor rotor. J Turbomach, 1998, 120: 131–140